An Improved Hybrid Field Model for Calculating On-Load Performance of Interior Permanent-Magnet Motors

Zhaokai Li, Xiaoyan Huang, *Member*, *IEEE*, Lijian Wu, *Senior Member, IEEE,* He Zhang, *Senior Member, IEEE*, Tingna Shi, *Member, IEEE,* Yan Yan, Bowen Shi, Geng Yang, *Member, IEEE*

***Abstract*—This paper develops an improved hybrid field model (IHFM) to predict the on-load performance of interior permanent-magnet (IPM) motors considering both iron saturation and slotting effect. It combines the air-gap analytical model based on modified conformal mapping with the reluctance mesh method for stator and rotor. The reluctance mesh method can accurately predict the rotor saturation and tooth-tip saturation even their field distribution is complicated due to armature reaction. Besides, IHFM will significantly accelerate computation speed using analytical model for air-gap region while keeping high accuracy. The finite-element analysis and experimental results of flat-type and V-type IPM motors are demonstrated to verify the effectiveness of the proposed model.**

***Index Terms*—Reluctance network, analytical model, conformal mapping, reluctance mesh method, interior permanent-magnet motor**

I. INTRODUCTION

THE IPM motor has the advantage of high torque, high power density and high efficiency. It has been widely used and investigated in the research and industrial application. For accurate prediction of IPM motors, FE analysis is one of the good choices because it can account for the nonlinearity of magnetic materials and therefore achieve high accuracy [1]. However, it consumes huge computation and lacks the insight for motor design.

In the stage of initial design and optimization, the circuit-based model and the analytical model are usually employed to save the calculation time. For the circuit-based model of IPM motors, magnetic equivalent circuit model (MECM) calculates its lumped parameter based on the division of regular flux path [2]-[5] while reluctance network method (RNM) defines the network reluctance (RN) according to the certain mesh rules [6]-[7]. Hence, MECM can save much computation when calculating the magnetic field with the regular flux path and RNM exhibits high accuracy regardless the complexity of field distribution. However, MECM has poor performance in calculating flux density along the irregular flux path (e.g. air-gap region and tooth-tip region) while RNM bears huge computational burden compared with MECM [8]. Besides, both circuit-based models have the disadvantage of reconstruction of circuit at different rotor position, which significantly increases the complexity to calculate time-varying performance.

As for analytical model, the winding function theory is widely-used to calculate the magnetic motive force (MMF) according to the winding distribution and obtain the air-gap inverse function [9]. [10]. [11]. The rotor MMF function is modified in [12] to account for the pole-cap effect. However, these methods neglect the magnetic saturation and show low accuracy.

The modified winding function combined with MECM is proposed in [13]-[16]. The flux line in the IPM motor at different rotor position is investigated to obtain the new equivalent air-gap function and computed the inductance under on-load condition [13]. Besides, the harmonic component of air-gap flux density considering PWM effect can be analyzed for magnet eddy-current loss calculation based on the combination of winding function and magnetic equivalent circuit (MEC) [14]. Elloumi *et al*. analyzed the flux weakening capability of IPM motors using modified winding function with simple MEC in dq-axis and obtained good prediction accuracy [16]. Compared to the original winding function model, these models have improved the calculation accuracy because they account for the magnetic potential drop in the iron region. However, the magnetic bridge saturation and tooth-tip saturation is too complex to be accurately modelled by simple MEC. Hence, an accurate stator and rotor permeance identification based on finite-element analysis was combined with winding function theory to show the accurate iron saturation [17].

Compared with the winding function model which is a one-dimension analytical model, the two-dimension analytical model based on Poisson or Laplace equation achieves higher accuracy for predicting air-gap field. It is extensively used in surface-mounted permanent magnet (SPM) motors due to the accurate modelling of PM in the air-gap region. The conformal mapping model based on one-pole-pitch region is proposed in [18] to predict the magnetic field of SPM motors. One-pole-pitch region is necessary for SPM motors because the PM equivalent current is placed inside the air-gap region. Nevertheless, it can be optimized to one-slot conformal mapping for IPM motors as the PM equivalent current is on the interface between rotor and air-gap. Hence, the calculation burden is decreased. For IPM motors, the complex permeance model combined with FEM-based slotless air-gap field is proposed in [1]. However, it neglects the deformation of circular path for predicting air-gap field and therefore introduces larger error with smaller slot opening. The MECM combined with analytical model based on complex permeance

function [19]-[20] or subdomain technique [21]-[24] has been investigated to consider the stator saturation. Nevertheless, the rotor saturation is neglected in these models for SPM motors.

Unlike the SPM motor whose PM produced field can be analytically calculated in [19]-[24], IPM motor cannot be directly analyzed using two-dimension analytical model since the rotor field distribution is complex and significantly affected by armature reaction. Mirazimi *et al.* proposed a conformal mapping model to represent the rotor saliency and stator slotting in the IPM motors. The air-gap field was calculated using conformal mapping technique but the bridge saturation is neglected [25]. With the aid of MECM, the rotor and stator saturation were included in the improved analytical model based on conformal mapping [26]-[27]. The subdomain-based analytical model for IPM motors is combined with MECM to accurately predict the electromagnetic performance in [28]-[29]. By applying the boundary condition between iron region and air-gap region, the iron permeability can be iteratively calculated for spoke-type IPM motors [28] and multilayer IPM motors [29]. However, these two-dimension analytical model in [26]-[29] can only analyze the open-circuit field of IPM motors. There are few papers about two-dimension analytical model for IPM motors under on-load condition due to the complex rotor saturation.

In this paper, a computationally efficient IHFM combining RNM and MECM is proposed to account for both slotting effect and saturation effect with high accuracy for IPM motors. The analytical air-gap field calculation based on one-slot conformal mapping is introduced to replace the large air-gap RN. Hence, the RN and MEC will stay unchanged at any rotor position, which simplifies the network modelling. In the IPM motors, the armature reaction field has significant influence on the rotor bridge saturation and tooth-tip saturation. Hence, a novel RNM is used to accurately capture the magnetic potential drop along the rotor and tooth surface while MECM is introduced for the modelling of rotor yoke, stator yoke and tooth body. IHFM makes the best of computation resource to analyze the IPM motors under on-load condition with high accuracy and low computation. Finite-element analysis and experiments of two IPM motors with flat-type rotor and V- type rotor has been carried out to validate the proposed model.

II. Improved Hybrid Field Model

There are two ways to look into the improved hybrid field model. In the view of a two-dimension analytical model, it incorporates the RNM and MECM to account for both PM-produced field and iron saturation. .As a modified circuit-based model, the large air-gap RN is replaced by flux sources using analytical air-gap solution, saving much calculation time and decreasing the complexity of network modelling. Fig. 1 shows the schematic of IHFM for analyzing IPM motors. The region division with different calculation method is given as follows: Region III (air-region) is represented by analytical solution based on one-slot conformal mapping; Region II (tooth edge) and Region IV (rotor surface) are modelled using RN; Region I (stator tooth and stator yoke) and Region V (rotor yoke) are calculated using MECM. The coupling between analytical model and RNM is based on equivalent transformation between the equivalent virtual surface current and magnetic potential drop on the interface of Region III.

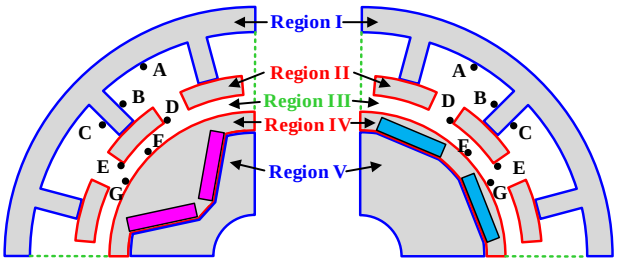

(a) V-type rotor (b) flat-type rotor

Fig. 1 The schematic of IPM motors using IHFM

A. Novel reluctance network

For IPM motors, the flux path in the rotor bridge and stator tooth-tip is irregular under on-load condition and they will significantly influence the air-gap field distribution. Hence a novel mesh cell is proposed to model these important regions with complex flux path, as shown in Fig. 2. Only three reluctances are used in the modular mesh cell with a flux source representing the air-gap field. The air-gap flux source is the key to incorporating the analytical model into the RNM. The rotation of rotor only changes the value of air-gap flux source and keeps the reluctance network unchanged. The air-gap flux is obtained from vector potential distribution

$$\phi_{ak} = l_{ef}(A_{z1} - A_{z2}) \tag{1}$$

where l_{ef} is the effective length of the IPM motor. The radial and tangential iron reluctance in the novel mesh cell is calculated by

$$\begin{aligned} G_{rr1} &= \frac{\mu_r \alpha_m l_{ef}}{\ln(r_2/r_1)} \\ G_{rt1} &= \frac{2\mu_r l_{ef} \ln(r_2/r_1)}{\alpha_m} \end{aligned} \tag{2}$$

where a_m is the angle of sectorial reluctance. r_1 and r_2 are the internal and external radius.

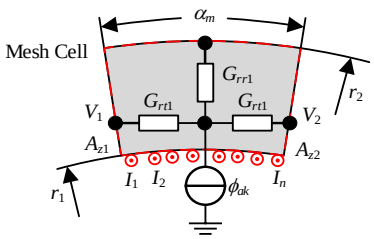

Fig. 2 The modular mesh cell for the reluctance network.

Based on the rectangular mesh method and novel mesh cell, the corresponding RN can be automatically generated without a priori knowledge of flux path. Hence, the proposed RNM representing stator tooth edge and rotor surface (red box in Fig. 3) can be determined according to (2). As the air-gap reluctances are replaced by flux source, the calculation time will be shortened. Besides, the proposed RN is applicable for every rotor position, which is different from the dynamic RNM [8] or MECM [3]. In the IHFM, the number of modular mesh cells in the pole-shoe region and along the rotor surface are selected according to the saturation level. For the rotor bridge region with high saturation, the criteria for the number of modular mesh cell is gives as $G_{rt1} >> G_{rr1}$ when using the same

iron permeance. As for the pole-shoe region, the criterion of $G_{rt1}<G_{rr1}$ is obtained based on the lower iron saturation. Such choice will reach a good compromise between calculation efficiency and accuracy.

As for Region I and Region V, their geometry is regular and the flux travels through these regions uniformly. Hence the MECM is proposed to calculate their magnetic potential distribution. In Fig. 3(a), the stator yoke reluctance G_{syk} and stator tooth reluctance G_{stk} can be expressed as [3]

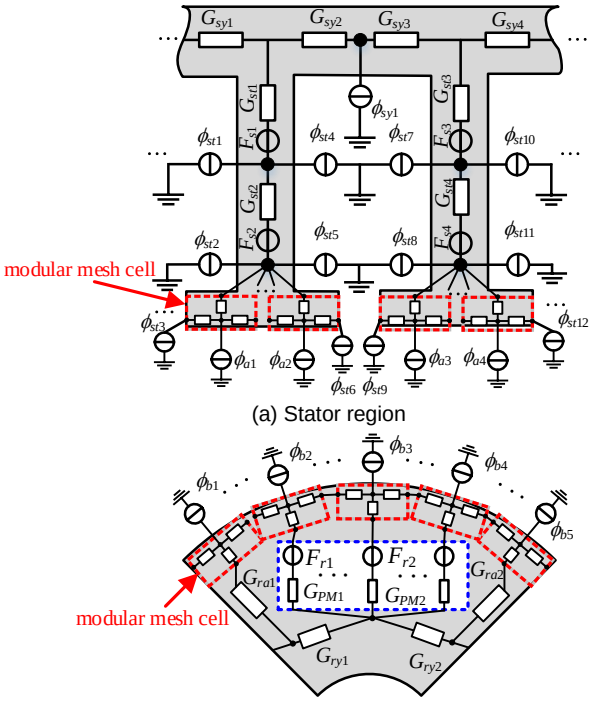

(a) Stator region

(b) Rotor region

Fig. 3 The RN and MEC for IPM motors.

$$G_{syk}=\frac{\mu_r l_{ef} Q_s \ln(R_3/(R_3-h_{sy}))}{\pi},\ k=1,2,\cdots$$
$$G_{stk}=\frac{\mu_r l_{ef} b_t}{2h_t},\qquad k=1,2,\cdots \tag{3}$$

where R_3 is the stator external radius and h_{sy} is the stator yoke height. Q_s is the slot number. b_t and h_t are the width and height of stator tooth. In Fig. 3(b), the PM reluctance G_{PMk} is calculated as [3]

$$G_{PMk}=\frac{\mu_r l_{ef} b_{PM}}{2h_{PM}},\quad k=1,2,\cdots \tag{4}$$

where b_{PM} and h_{PM} are the width and height of PM. The rotor yoke iron G_{ryk} and the iron between PM G_{rak} is considered as trapezoidal and therefore they are expressed as

$$G_{rak}=\frac{\mu_r l_{ef}(a_{trap}-b_{trap})}{h_{trap}\ln(a_{trap}/b_{trap})},\qquad k=1,2,\cdots$$
$$G_{ryk}=\frac{\mu_r l_{ef} h_{trap}\ln(a_{trap}/b_{trap})}{(a_{trap}-b_{trap})},\quad k=1,2,\cdots \tag{5}$$

where a_{trap}, b_{trap} and h_{trap} are the bases and height of trapezoidal iron. The calculation of magnetic voltage source in the stator and rotor can be seen in [8].

For the slot region with air permeability, its analytical solution can be directly obtained. Therefore, the slot flux source flowing into the stator teeth and stator yoke is proposed to improve the accuracy rather than MECM, as shown in Fig. 3(a). It is calculated by

$$\phi_{st}=l_{ef}(A_{zstk}-A_{zst(k+1)})$$
$$\phi_{sy}=l_{ef}(A_{zsyk}-A_{zsy(k+1)}) \tag{6}$$

where A_{zsyk} and A_{zstk} are the vector potential on the slot bottom and on the left/right side of slot region.

B. Analytical model for air-gap region

The keypoint of the improved hybrid field model is the accurate prediction of air-gap field. The analytical model based on one-slot conformal mapping is proposed to calculate the air-gap field distribution instead of RNM while achieving high accuracy. The calculation speed will be significantly improved as the magnetic potential node is decreased. Besides, the dynamic construction of RN is avoided to reduce the modelling complexity. To obtain the analytical air-gap field solution of the IPM motor, the general boundary condition between air-gap region and iron region with different permeability is listed as

$$\begin{cases} B_{r\_air}=B_{r\_iron} \\ H_{t\_air}-H_{t\_iron}=K_{iron} \end{cases} \tag{7}$$

Under normal circumstances, there is no surface current sheet and therefore K_{iron}=0, as shown in Fig. 4(a). In this paper, the equivalent virtual current sheet K_{iron} is introduced to represent the PMs, winding current and iron saturation. To keep the air-gap field unchanged and avoid calculating the permeability of the iron in the analytical model, H_{t_iron} are replaced by K_{iron}, as shown in Fig. 4(b). It is noted that the permeability of iron becomes infinite after the transformation as H_{t_iron}=0. Hence, the modified boundary condition is shown as

$$\begin{cases} B_{r\_air}=B_{r\_iron} \\ H_{t\_air}=K_{iron} \end{cases} \tag{8}$$

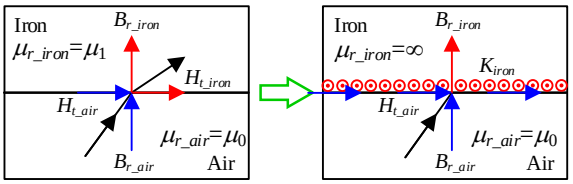

(a) (b)

Fig. 4 The (a) original and (b) modified boundary condition for IHFM

In order to solve governing Laplace equation for the air-gap region using conformal mapping model, surface current sheet K_{iron} in (8) can be regarded as uniformly distributed dot currents for simplicity, as shown in Fig. 4 (b). Based on the Ampere's law, the dot currents is calculated by [20]-[21]

$$I_1=I_2=\cdots=I_n=\frac{V_1-V_2}{n} \tag{9}$$

where V_1 and V_2 are obtained from the mesh cell of Fig. 2. Accordingly, the equivalent dot currents along the rotor surface, which represents the PM and rotor saturation, can be equivalently calculated from magnetic potential distribution of modular mesh cells on the rotor surface, as shown in Fig. 3(b).

Unlike the SPM motor whose PM equivalent current is

located along the PM edge in the air-gap and should be transformed at every rotor position using exact conformal mapping [31], the PM equivalent current of IPM motor is placed on the rotor surface and stays unchanged at any rotor position. Therefore, the conformal mapping calculation is required only at the initial rotor position. Much calculation will be saved compared with the analytical calculation in SPM motor.

In the proposed IHFM, five transformations are used to convert the slotted annular domain to the rectangular domain for air-gap region using the simplified one-slot model, as shown in Fig. 5. Take the position $r_s e^{j*\alpha s}$ in the complex plane of original S domain as an example, it will be transformed to z_{full} in the Z_{full} domain using the logarithmic mapping, as show in Fig. 5(a)-(b), where $z_{full}=\log(r_s)+j*\alpha_s$ Then the position z_{full} is transformed to z_{slot} corresponding to Fig. 5(b)-(c) using the following equation

$$\begin{aligned} z_{slot} &= \mathrm{Re}(z_{full}) + i*(\mathrm{Im}(z_{full})\%(2\pi/Q_s)) \\ &= \log(r) + i*(a\%(2\pi/Q_s)) \end{aligned} \tag{10}$$

Next, the position z_{slot} in the polygon of Z_{slot} domain can be transformed to the position w_{slot} in the rectangle of W_{slot} domain using the inverse Schwarz-Christoffel (SC) mapping [32].

$$z_{slot} = A_0 \int \prod_{k=1}^{n-1} (w_{slot} - w_k)^{-\frac{\alpha_k}{\pi}-1} dw + C_0 \tag{11}$$

Since it is difficult to directly solve the SC parameter in the mapping, the SC Toolbox is employed to calculate the position w_{slot} in the W_{slot} domain, as shown in Fig. 5(c)-(d). It is noted that SC mapping is the most time-consuming transformation as it requires numerical calculation of nonlinear equation. However, by simplifying the multi-slots model to one-slot model, the calculation speed will be significantly improved. Then based on the periodicity of (10), the position w_{full} is obtained from w_{slot} using (12) for Fig. 5(d)-(e).

$$\begin{aligned} w_{full} = &\left[Q_s - 1 - \left\lfloor \mathrm{Im}(z_{full}) / (2\pi/Q_s) \right\rfloor \right] * w_a \\ &+ \mathrm{Re}(w_{slot}) + i * \mathrm{Im}(w_{slot}) \end{aligned} \tag{12}$$

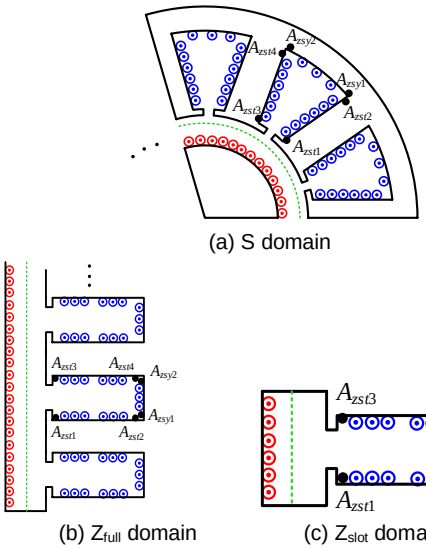

(a) S domain

(b) Z_{full} domain (c) Z_{slot} domain

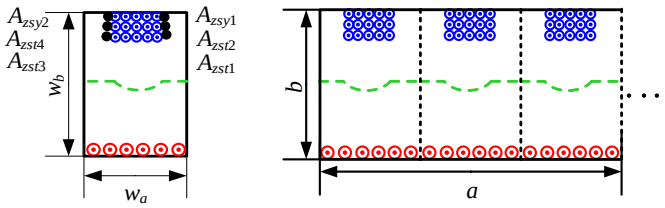

(d) W_{slot} domain (e) W_{full} domain

Fig. 5 The conformal mapping model based on one-slot region.

Based on these transformations, both current position and the path of magnetic field can be determined in the S domain and W_{full} domain. Hence, the vector potential $A_z(x, y)$ produced by the dot current $i_0(x_c, y_c)$ in the rectangular W_{full} domain can be calculated as [33]

$$\begin{aligned} A_z(x,y) = \frac{\mu_0 i_0}{2\pi} \Big\{ &\ln \left| e^{-c_\omega (ix+y+b/2)} - e^{-c_\omega (ix_c+y_c+b/2)} \right| \\ &- \sum_{k=1}^{+\infty} \frac{\cosh(c_\omega k(y-b)) + e^{kc_\omega(2y_c-b)} \cosh(kc_\omega y)}{k \sinh(kc_\omega b)} \\ &e^{-c_\omega k y_c} \cos\left[c_\omega k (x - x_c) \right] \Big\} \end{aligned} \tag{13}$$

where $c_w=2\pi/a$, $a=Q_s*w_a$, $b=w_b$. w_a and w_b are the length and width of rectangle in W_{slot} domain. The flux densities in x and y direction are calculated according to the vector potential in the W_{full} domain

$$\begin{aligned} B_{x_w} &= \frac{\partial A_z(x,y)}{\partial y} \\ B_{y_w} &= -\frac{\partial A_z(x,y)}{\partial x} \end{aligned} \tag{14}$$

Based on the conformal mapping theory, the magnetic field in x and y direction of the S domain can be calculated from that in the W_{full} domain

$$B_s = B_{xs} + jB_{ys} = B_W \lambda_0 = (B_{x_w} + jB_{y_w})\lambda_0 \tag{15}$$

where the complex permeance function λ_0 is expressed as

$$\lambda_0 = \frac{1}{\dfrac{\partial z}{\partial w}} \frac{1}{r_s e^{j\alpha_s}} \tag{16}$$

where $\frac{\partial z}{\partial w}$ is obtained from the SC transformation.

C. Improved hybrid field model

The magnetic field of IPM motors cannot be determined directly, because the analytical air-gap field solution requires the equivalent dot current from the magnetic potential distribution in the proposed RNM while the node flux source $\mathbf{\Phi}$ in the RNM is calculated from the air-gap field distribution. Hence, a solving loop is required to obtain the saturation level of stator and rotor iteratively. The solution of magnetic potential distribution $\mathbf{V}$ in the nonlinear RN and MEC can be obtained according to Kirchhoff's law.

$$f(\mathbf{V}) = \mathbf{A}\mathbf{\Lambda}\mathbf{A}^{\mathrm{T}}\mathbf{V} - \mathbf{A}\mathbf{\Lambda}\mathbf{F}_{\mathbf{sr}} - \mathbf{\Phi} = 0 \tag{17}$$

where $\mathbf{\Phi}=[\phi_{a1},\cdots,\phi_{sy1},\cdots,\phi_{st1},\cdots,\phi_{b1},\cdots]$. $\mathbf{A}$ is incidence matrix obtained from the RN and MECM. $\mathbf{F_{sr}}$ consists of the magnetic voltage drop from PM and winding current. $\mathbf{\Lambda}$ represents the iron reluctance matrix. As shown in Fig. 6, $\mathbf{\Lambda}$ and $\mathbf{V}$ will be iteratively solved. Hence, the magnetic field of IPM motors can

be obtained at any rotor position by modifying the rotor position in (10)-(13).

The flux linkage of each phase is calculated from the air-gap vector potential

$$\Psi_{ABC} = N_c \sum_{k=1}^{N_p} l_{ef} \left[A_{zk}(R_s, \alpha_1) - A_{zk}(R_s, \alpha_1 + 2\pi\tau/Q_s) \right] \quad (18)$$

where R_s is the stator outer radius. τ is the slot pitch. N_p is the pair of slot for each phase. α_1 and N_c are the initial angle of the coil and the number of coil belonging to each phase, respectively. Hence, the induced voltage of the IPM motor is expressed as

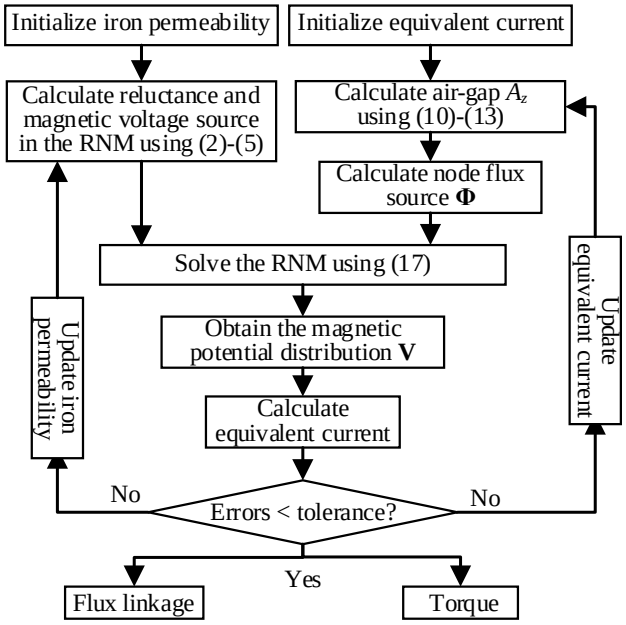

Fig. 6 The flowchart of solving process for any rotor position.

$$U_{ABC} = \frac{d\Psi_{ABC}}{dt} \quad (19)$$

The electromagnetic torque is calculated according to the Maxwell tensor theory using the radial and Tangential flux density in the air-gap

$$T_e = r l_{ef} \int_0^{2\pi} B_{r\_air}(r,\alpha) B_{t\_air}(r,\alpha) d\alpha \quad (20)$$

where α and r are the angle and radius of the circular integral path along the middle of air-gap region.

III. FE Analysis and Experiment

In this paper, an 8-pole/36-slot V-type IPM motor and a 4-pole/24-slot flat-type IPM motor are designed and analyzed to validate the proposed model, as shown in Fig. 7. The IHFM predictions are compared with FEM results and the experiment is carried out to show the calculation accuracy. The two prototype motors are shown in Figs. 7-9 and their main parameters are displayed in Table I. The nonlinear BH curves of the iron material is shown in Fig. 10. It is noted that the average flux density in the rotor bridge of both IPM motors is larger than 2.2T at rated load, which can be regarded as highly saturated, as shown in Fig. 7.

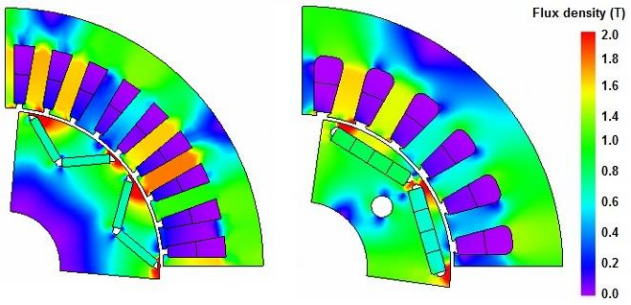

(a) V-type rotor (b) flat-type rotor

Fig. 7 The field distribution of IPM motors at rated load.

(a) V-type rotor (b) Stator

Fig. 8 The prototype 8-pole/36-slot V-type IPM motors.

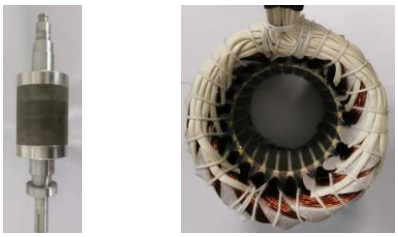

(c) flat-type rotor (d) Stator

Fig. 9 The prototype 4-pole/24-slot flat-type IPM motors.

TABLE I
THE MAIN PARAMETERS OF IPM MOTOS

Parameter	V-type IPM machine	flat-type IPM machine
Stator outer diameter	120mm	245mm
Magnet material	N35UH	N38H
Iron material	20JNEH1200	M235-35A
Rated speed	15000rpm	2800rpm

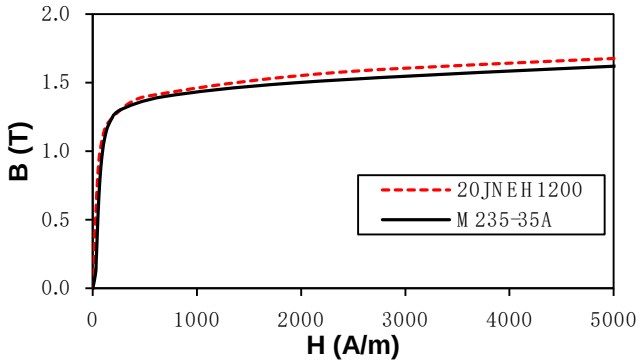

Fig. 10 The BH curves of magnetic material for IPM motors.

The interaction between slots is negligible due to the symmetrical structure of stator and therefore the one-slot conformal mapping model has same results as those from the exact conformal mapping which transformed the whole air-gap region in the SC mapping. Besides, the accuracy of the one-slot conformal mapping model is compared with FEM calculations

neglecting saturation effect. As shown in Fig. 1, seven dot currents locating in "A-G" are chosen to calculate magnetic field in the middle of air-gap using one-slot conformal mappings and FEM, respectively. The average error for radial and tangential air-gap field of V-type IPM motor is less than 0.2% and 0.3%, as shown in Table II. As for flat-type IPM motor, they are less than 0.2% and 0.5% according to Table III. It is noted that the variation of slot opening has negligible influence on the accuracy of one-slot conformal mapping.

The saturation effect is investigated using IHFM. For the V-type IPM motor, there are 160 and 400 modular mesh cells for pole-shoe region and rotor surface, respectively. As for flat-type IPM motor, they become 80 and 168, respectively.

TABLE II
THE AVERAGE ERROR OF MAGNETIC FIELD USING ONE-SLOT CONFORMAL MAPPING FOR V-TYPE IPM MOTOR (UNIT: %)

Slot opening	Flux density	A*	B*	D*	F*	G*
0.5mm	Radial	0.15	0.15	0.16	0.14	0.15
	Tangential	0.17	0.13	0.15	0.11	0.11
1mm	Radial	0.14	0.14	0.14	0.13	0.14
	Tangential	0.15	0.17	0.15	0.12	0.15
2mm	Radial	0.18	0.18	0.20	0.13	0.19
	Tangential	0.21	0.21	0.22	0.15	0.15
3mm	Radial	0.14	0.14	0.15	0.12	0.15
	Tangential	0.22	0.22	0.26	0.15	0.19
4mm	Radial	0.11	0.11	0.13	0.08	0.12
	Tangential	0.26	0.26	0.29	0.17	0.17

* The position "A-G" are defined in Fig. 1.

TABLE III
THE AVERAGE ERROR OF MAGNETIC FIELD USING ONE-SLOT CONFORMAL MAPPING FOR FLAT-TYPE IPM MOTOR (UNIT: %)

Slot opening	Flux density	A	B	D	F	G
0.5mm	Radial	0.10	0.10	0.10	0.11	0.10
	Tangential	0.09	0.09	0.09	0.11	0.11
1mm	Radial	0.09	0.09	0.10	0.11	0.09
	Tangential	0.13	0.13	0.13	0.13	0.13
2mm	Radial	0.04	0.04	0.05	0.08	0.05
	Tangential	0.38	0.38	0.28	0.22	0.23
3mm	Radial	0.07	0.07	0.08	0.09	0.09
	Tangential	0.49	0.49	0.49	0.28	0.25

The V-type IPM motor is operated with current angle of 20º and the input current is 200A. The flat-type IPM motor runs using MTPA control, whose current angle is 16º and the input current is 47A. Under this load condition, the flux densities of both IPM motors are calculated using IHFM in Figs. 10-11, and their results show great agreement with FEM calculations.

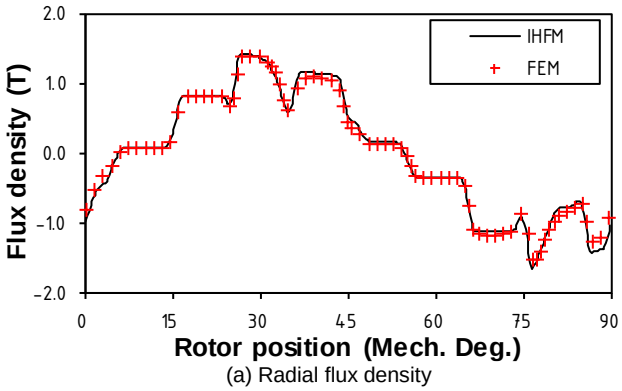

(a) Radial flux density

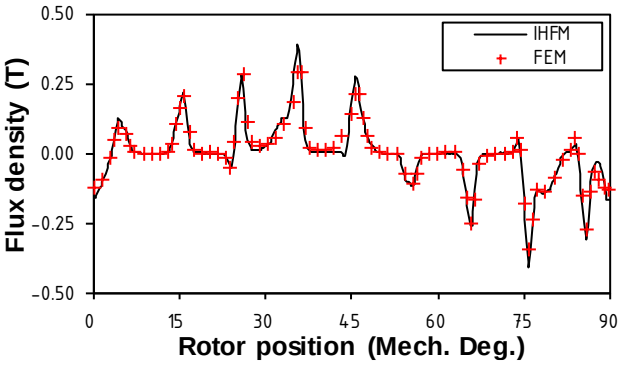

(b) Tangential flux density

Fig. 11 The air-gap filed distribution of V-type IPM motor at 164 N*m.

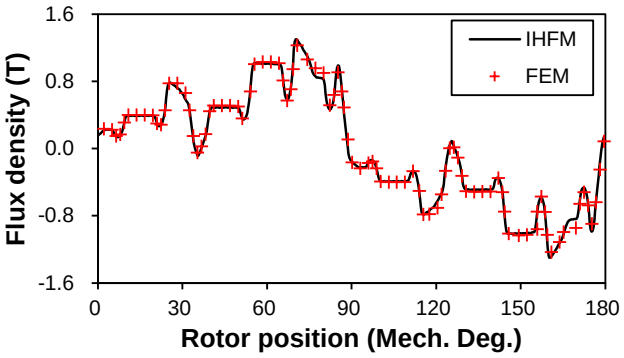

(a) Radial flux density

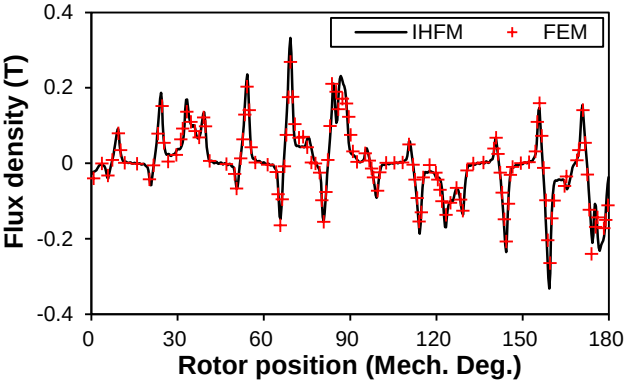

(b) Tangential flux density

Fig. 12 The air-gap filed distribution of flat-type IPM motor at 8.7N*m.

The flux linkage and induced voltage of both IPM motors using IHFM are consistent with FEM results under on-load condition, as shown in Figs. 13-16. The average errors of flux linkage using IHFM for V-type and flat-type IPM motors are 1.9% and 2.5%, respectively. As for the induced voltage, the average errors for V-type and flat-type IPM motors are 3.3% and 2.2%, respectively. Hence, it is demonstrated that the IHFM can accurately predict the induced voltage of IPM motors considering the armature reaction.

In Fig. 17, the torque waveforms using IHFM is similar to FEM calculations, the average torque error for V-type IPM motors is less than 0.5%. In Fig. 18, IHFM predicts higher torque value than FEM prediction, however it should be noted that the average torque error of IHFM prediction is less than 1.7%, which is rather small and acceptable. The differences of electromagnetic performance calculation using IHFM and FEM

come from the simplification of iron modelling using MECM and RNM to achieve high computational efficiency.

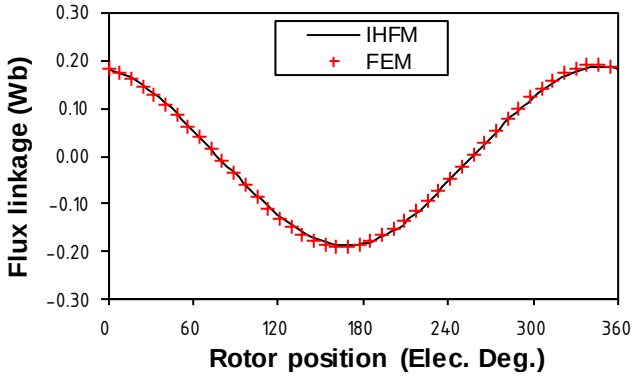

Fig. 13 The flux linkage waveform of V-type IPM motor at 164 N*m with current angle of 20º.

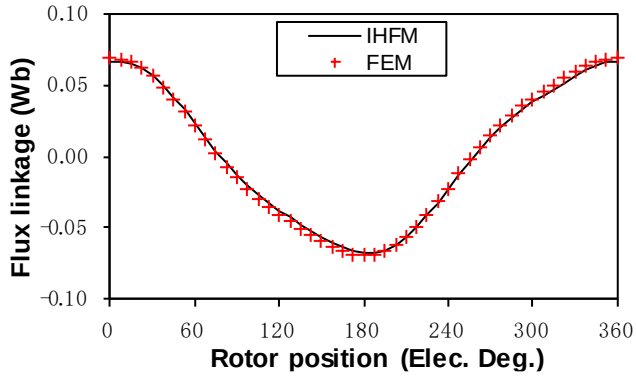

Fig. 14 The flux linkage waveform of flat-type IPM motor at 8.7N*m using MTPA control.

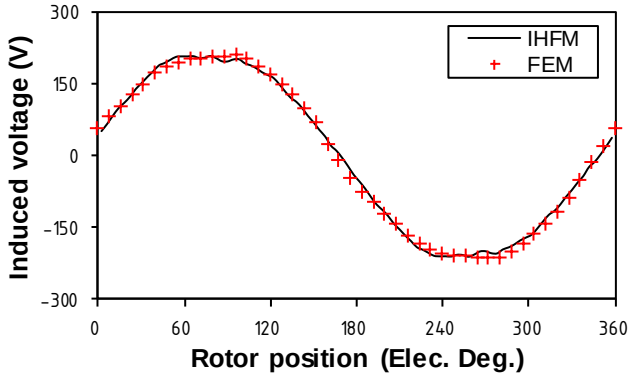

Fig. 15 The induced voltage waveform of V-type IPM motor at 164 N*m with current angle of 20º.

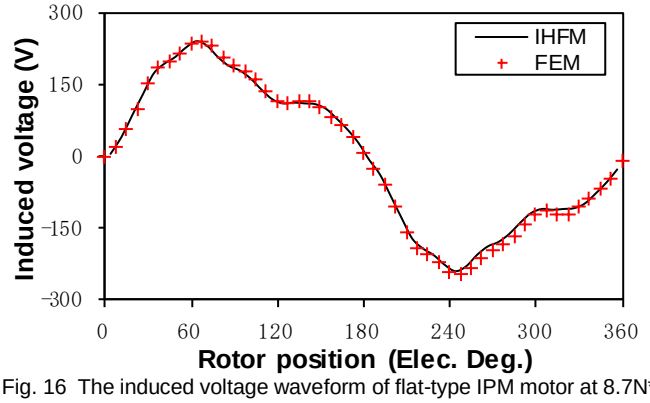

Fig. 16 The induced voltage waveform of flat-type IPM motor at 8.7N*m using MTPA control.

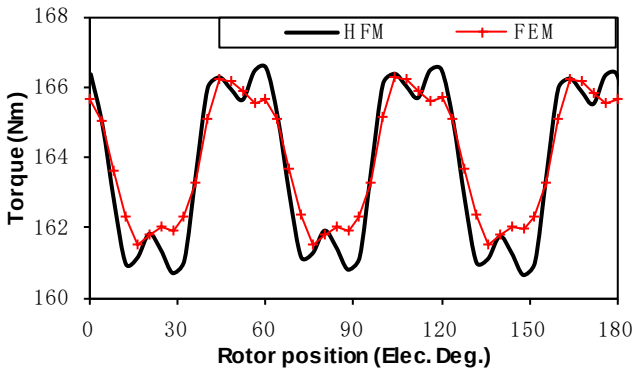

Fig. 17 The torque waveform of V-type IPM motor at 164 N*m with current angle of 20º.

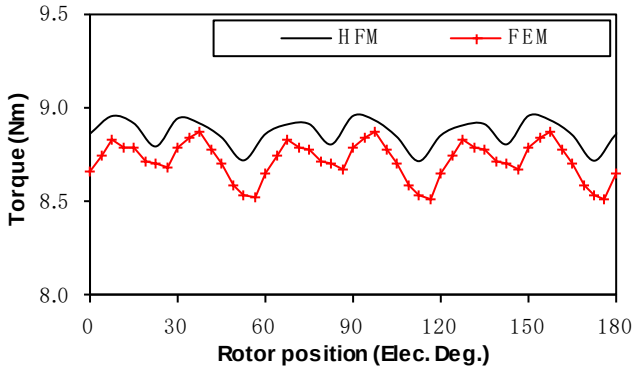

Fig. 18 The torque waveform of flat-type IPM motor at 8.7N*m using MTPA control.

In order to investigate the influence of armature field on the induced voltage and electromagnetic torque, IHFM is employed to calculate the magnetic field of IPM motors under different load condition. The flat-type IPM motor is operated using MTPA control strategy while V-type IPM motor runs with current angle of 20°. The major and 3rd harmonic voltage are calculated using IHFM for both IPM motors, as shown in Figs. 18-19. IHFM predictions agree well with FEM results, which means the proposed model can accurately describe the induced voltage. The average torque under different load condition is calculated for both IPM motors in Figs. 20-21. Both FEM calculations and experimental results are close to IHFM predictions regardless of the amplitude of winding current. The torque error of IHFM is less than 5% for both IPM motors according to the experiment results.

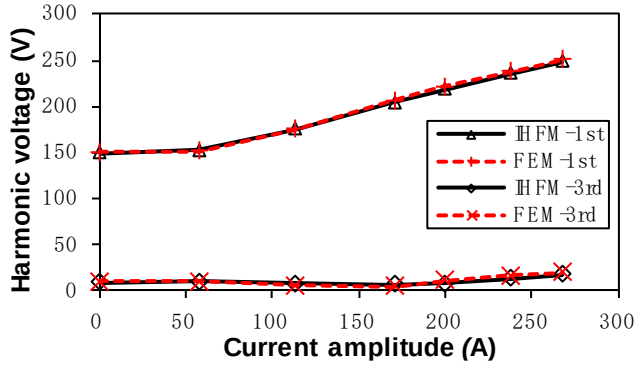

Fig. 19 The variation of induced harmonic voltage with the phase current amplitude using current angle of 20º for V-TYPE IPM motor.

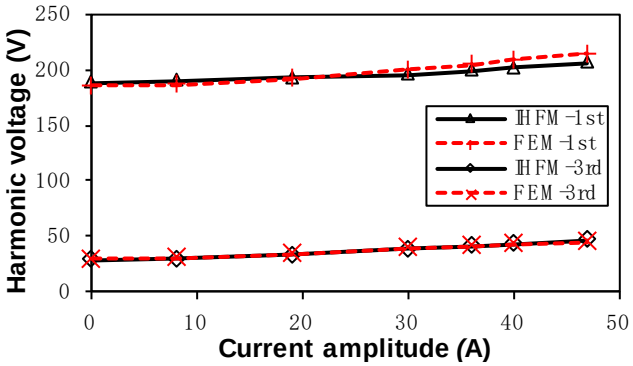

Fig. 20 The variation of induced harmonic voltage with the phase current amplitude using MTPA control for flat-type IPM motor.

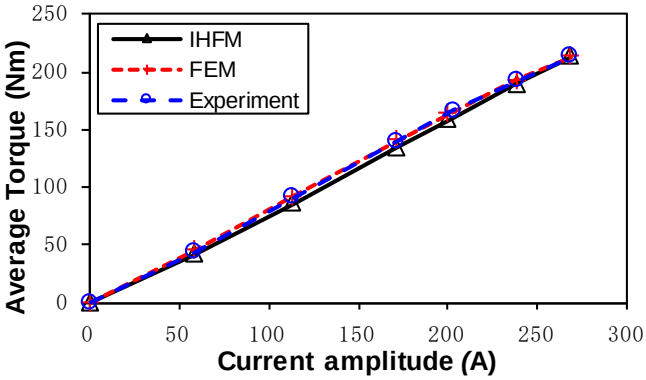

Fig. 21 The variation of average torque with the phase current amplitude using current angle of 20º for V-type IPM motor.

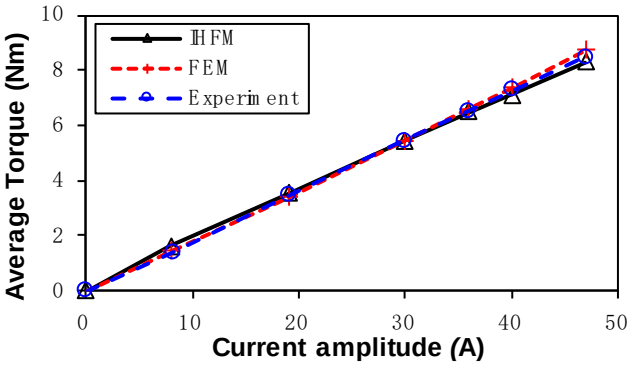

Fig. 22 The variation of average torque with the phase current amplitude using MTPA control for flat-type IPM motor.

The IPM motors is operated using i_d=0 control to verify the proposed model under different control strategy. The experiment is carried out for V-type IPM motor and its result compared with IHFM and FEM calculations in Fig. 23. The torque error is less than 5%, which shows the high accuracy of IHFM under i_d=0 operation. Besides, Fig. 24 shows that the IHFM can accurately predict the torque for flat-type IPM motor using i_d=0 control and the torque error is less than 5%.

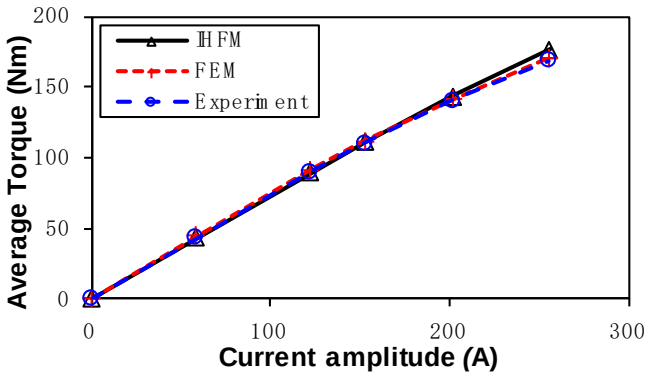

Fig. 23 The variation of average torque with the phase current amplitude using i_d=0 control for V-type IPM motor.

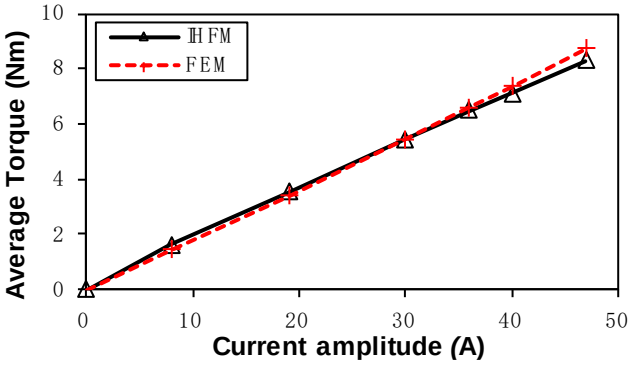

Fig. 24 The variation of average torque with the phase current amplitude using i_d=0 control for flat-type IPM motor.

Besides, the IHFM shows great accuracy in calculating the torque at different current angle for both IPM motors, as shown in Figs. 25-26. The average error of IHFM prediction for V-type IPM motor is less than 1.9% while it is less than 4.5% for flat-type IPM motor. Larger errors are observed for flat-type IPM motor due to the simplified modelling of iron region between PMs using MECM, which can be much saturated when current angle is large and therefore significantly influences the torque. As for V-type IPM motor, the iron region between PMs is large enough to avoid saturation regardless of the current angle. Hence, it can be concluded that the IHFM is suitable to calculate the torque-angle performances for IPM motors with large iron region between PMs or to calculate the torque characteristic of IPM motors using MTPA control. The work of analytical modeling for IPM motors with small iron region between PMs using flux-weakening control will be presented in the future.

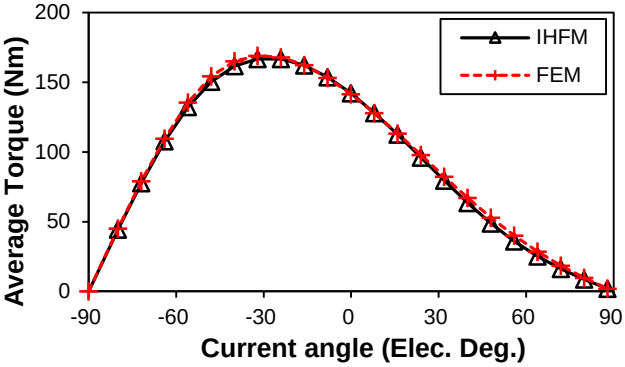

Fig. 25 The variation of average torque with the current angle for V-type IPM motor.

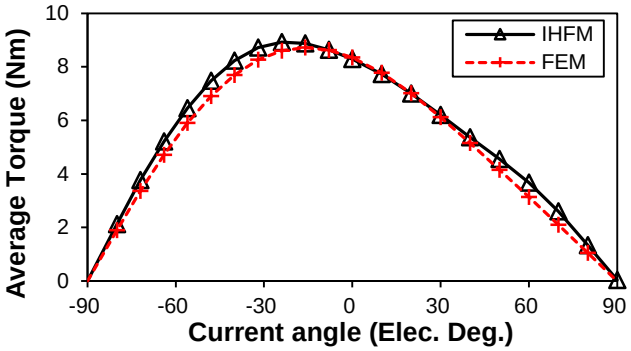

Fig. 26 The variation of average torque with the current angle for flat-type IPM motor.

The time efficiency is compared in Tables IV-VI. The same parameters are set to utilize IHFM in the Matlab platform and FEM in the JMAG, respectively, as shown in Table IV. In Table V, the IHFM consumes less than 1/10 the calculation time using FEM for V-type IPM motor. Besides, the calculation time using IHFM is less than 1/8 of that using FEM for flat-type IPM motor, as shown in Table VI. Hence IHFM has great advantage in calculation speed compared with FEM.

TABLE IV
SIMULATION SETTING FOR IPM MOTORS

IPM motor	Model	Air-gap division	Calculation steps	Total Node	Air-gap Node
V-type	IHFM	180	90	269	0
	FEM			2916	720
flat-type	IHFM	288	96	320	0
	FEM			5410	1151

TABLE V
CALCULATION TIME OF IHFM AND FEM FOR V-TYPE IPM MOTOR

Current (A)	0	57.7	113	171	200	238	268
HFM (s)	71	76	81	94	99	117	126
FEM (s)	1106	1174	1182	1223	1243	1278	1294

TABLE VI
CALCULATION TIME OF IHFM AND FEM FOR FLAT-TYPE IPM MOTOR

Current (A)	0	8	19	30	36	40	47
HFM (s)	94	102	103	103	112	115	117
FEM (s)	898	903	903	906	917	926	940

IV. CONCLUSION

This paper develops an improved hybrid field model for predicting on-load electromagnetic performance of IPM motors. Both MECM and RNM are used to represent the iron region in terms of the calculation accuracy and calculation time. The equivalent virtual currents calculated from the magnetic potential drop in the iron region are introduced to obtain the analytical air-gap solution. Meanwhile, the novel mesh cell with air-gap flux source from analytical model will form the RN and MEC of stator and rotor efficiently. The analytical model based on one-slot conformal mapping is proposed to improve the efficiency of calculation. Owing to the stationary air-gap region in IPM motors, conformal mapping is required only once while considering the position change of equivalent virtual current and the path in the transformation of air-gap region. Both FEM calculation and experimental results of flat-type and V-type IPM motors demonstrate the high accuracy of IHFM with reduced computational burden to the greatest extent.

REFERENCES

[1] B. Guo, Y. Huang, F. Peng, and J. Dong, "A new hybrid method for magnetic field calculation in IPMSM accounting for any rotor configuration," *IEEE Trans. Ind. Electron.*, vol. 66, no. 7, pp. 5015-5024, 2019.

[2] L. Zhu, S.Z. Jiang, Z.Q. Zhu, and C.C. Chan, "Analytical modeling of open-circuit air-gap field distributions in multisegment and multilayer interior permanent-magnet machines," *IEEE Trans. Magn.*, vol. 45, no. 8, pp. 3121-3130, 2009.

[3] X. Huang, M. Zhu, W. Chen, J. Zhang, and Y. Fang, "Dynamic reluctance mesh modeling and losses evaluation of permanent magnet traction motor," *IEEE Trans. Magn.*, vol. 6, no. 53, 2017.

[4] K. Nakamura, K. Saito, and O. Ichinokura, "Dynamic analysis of interior permanent magnet motor based on a magnetic circuit model," *IEEE Trans. Magn.*, vol. 39, no. 5, pp. 3250-3252, 2003.

[5] H. Yeo, D. Lim, and H. Jung, "Magnetic equivalent circuit model considering the overhang structure of an interior permanent-magnet machine," *IEEE Trans. Magn.*, vol. 55, no. 6, pp. 1-4, 2019.

[6] G. Liu, Y. Wang, Q. Chen, G. Xu, and D. Cao, "Design and analysis of a new equivalent magnetic network model for IPM machines," *IEEE Trans. Magn.*, vol. 56, no. 6, pp. 1-12, 2020.

[7] Shan Jiang, Guohai Liu, Wenxiang Zhao, Liang Xu, and Qian Chen, "Modeling and analysis of spoke-type permanent magnet vernier machine based on equivalent magnetic network method," Chinese Journal of Electrical Engineering, vol. 4, no. 2, pp. 96-103, 2018.

[8] G. Liu, S. Jiang, W. Zhao and Q. Chen, "Modular reluctance network simulation of a linear permanent-magnet vernier machine using new mesh generation methods," *IEEE Trans. Ind. Electron.*, vol. 64, no. 7, pp. 5323-5332, 2017.

[9] T.A. Lipo, "Analysis of synchronous machine,", Madison, WI: Univ. Wisconsin, 2008.

[10] K. Kim, J. Park, J. Hur, and B. Kim, "Comparison of the fault characteristics of IPM-type and SPM-type BLDC motors under inter-turn fault conditions using winding function theory," *IEEE Trans. Ind. Appl.*, vol. 50, no. 2, pp. 986-994, 2014.

[11] H. Chen, D. Li, R. Qu, Z. Zhu and J. Li, "An improved analytical model for inductance calculation of interior permanent magnet machines," *IEEE Trans. Magn.*, vol. 50, no. 6, pp. 1-8, 2014.

[12] Q. Li, T. Fan, and X. Wen, "Armature-reaction magnetic field analysis for interior permanent magnet motor based on winding function theory," *IEEE Trans. Magn.*, vol. 49, no. 3, pp. 1193-1201, 2013.

[13] M. Farshadnia, M. Cheema, R. Dutta, and J.E. Fletcher, "Analytical modeling of armature reaction air-gap flux density considering the non-homogeneously saturated rotor in a fractional-slot concentrated-wound ipm machine," *IEEE Trans. Magn.*, vol. 53, no. 2, pp. 1-12, 2017.

[14] A. Balamurali, C. Lai, A. Mollaeian, V. Loukanov, and N. Kar, "Analytical investigation into magnet eddy current losses in interior permanent magnet motor using modified winding function theory accounting for pulsewidth modulation harmonics," *IEEE Trans. Magn.*, vol. 52, no. 7, pp. 1-5, 2016.

[15] H. Gurleyen and E. Mese, "A nonlinear q-axis inductance modeling of a 12-slot 10-pole IPM using approximate analytical methods," *IEEE Trans. Energy Convers.*, vol. 35, no. 2, pp. 621-630, 2020.

[16] N. Elloumi, M. Bortolozzi, A. Masmoudi, M. Mezzarobba, M. Olivo and A. Tessarolo, "Numerical and analytical approaches to the modeling of a spoke type IPM machine with enhanced flux weakening capability," *IEEE Trans. Ind. Appl.*, vol. 55, no. 5, pp. 4702-4714, 2019.

[17] A. Tessarolo, "Accurate computation of multiphase synchronous machine inductances based on winding function theory," *IEEE Trans. Energy Convers.*, vol. 27, no. 4, pp. 895-904, 2012.

[18] K. Ramakrishnan, D. Zarko, A. Hanic, and G. Mastinu, "Improved method for field analysis of surface permanent magnet machines using Schwarz–Christoffel transformation," *IET Electr. Power App.*, vol. 11, no. 6, pp. 1067-1075, Jun 2017.

[19] L.J. Wu, Z. Li, X. Huang, Y. Zhong, Y. Fang and Z.Q. Zhu, "A hybrid field model for open-circuit field prediction in surface-mounted pm machines considering saturation," *IEEE Trans. Magn.*, vol. 54, no. 6, pp. 1-12, 2018.

[20] L.J. Wu, Z. Li, D. Wang, H. Yin, X. Huang and Z.Q. Zhu, "On-load field prediction of surface-mounted pm machines considering nonlinearity

based on hybrid field model," *IEEE Trans. Magn.*, vol. 55, no. 3, pp. 1-11, 2019.
[21] L. Wu, H. Yin, D. Wang and Y. Fang, "A nonlinear subdomain and magnetic circuit hybrid model for open-circuit field prediction in surface-mounted pm machines," *IEEE Trans. Energy Convers.*, vol. 34, no. 3, pp. 1485-1495, 2019.
[22] L. Wu, H. Yin, D. Wang, and Y. Fang, "On-load field prediction in spm machines by a subdomain and magnetic circuit hybrid model," *IEEE Trans. Ind. Electron.*, vol. 67, no. 9, pp. 7190-7201, Sept. 2020.
[23] P. Liang, F. Chai, Y. Li and Y. Pei, "Analytical prediction of magnetic field distribution in spoke-type permanent-magnet synchronous machines accounting for bridge saturation and magnet shape," *IEEE Trans. Ind. Electron.*, vol. 64, no. 5, pp. 3479-3488, May 2017.
[24] P. Liang, F. Chai, Y. Yu and L. Chen, "Analytical model of a spoke-type permanent magnet synchronous in-wheel motor with trapezoid magnet accounting for tooth saturation," *IEEE Trans. Ind. Electron.*, vol. 66, no. 2, pp. 1162-1171, Feb. 2019.
[25] M.S. Mirazimi and A. Kiyoumarsi, "Magnetic field analysis of multi-flux-barrier interior permanent-magnet motors through conformal mapping," *IEEE Trans. Magn.*, vol. 53, no. 12, pp. 1-12, 2017.
[26] D. Lim, K. Yi, D. Woo, H. Yeo, J. Ro, C. Lee, and H. Jung, "Analysis and design of a multi-layered and multi-segmented interior permanent magnet motor by using an analytic method," *IEEE Trans. Magn.*, vol. 50, no. 6, pp. 1-8, 2014.
[27] Z. Li, X. Huang, L. Wu, T. Long, B. Shi, and H. Zhang, "Open-circuit field prediction of interior permanent-magnet motor using hybrid field model accounting for saturation," *IEEE Trans. Magn.*, vol. 55, no. 7, pp. 1-7, 2019.
[28] P. Liang, F. Chai, Y. Bi, Y. Pei, and S. Cheng, "Analytical model and design of spoke-type permanent-magnet machines accounting for saturation and nonlinearity of magnetic bridges," *J. Magn. Magn. Mater.*, vol. 417, pp. 389-396, 2016.
[29] Z. Zhang, C. Xia, Y. Yan, Q. Geng and T. Shi, "A hybrid analytical model for open-circuit field calculation of multilayer interior permanent magnet machines," *J. Magn. Magn. Mater.*, vol. 435, pp. 136-145, 2017.
[30] Z. Li, X. Huang, L. Wu, T. Long, B. Shi, and H. Zhang, "Open-circuit field prediction of interior permanent-magnet motor using hybrid field model accounting for saturation," *IEEE Trans. Magn.*, vol. 55, no. 7, pp. 1-7, 2019.
[31] A. Hanic, D. Zarko, D. Kuhinek, and Z. Hanic, "On-load analysis of saturated surface permanent magnet machines using conformal mapping and magnetic equivalent circuits," *IEEE Trans. Energy Convers.*, pp. 1-10, 2017.
[32] Tim C. O'Connell and P.T. Krein, "A Schwarz-Christoffel-based analytical method for electric machine field analysis," *IEEE Trans. Energy Convers.*, vol. 24, no. 3, pp. 565-577, 2009.
[33] B. Hague, "The principles of electromagnetism applied to electrical machines,", New York: Dover Publications, 1962.

Zhaokai Li was born in Lishui, China, in 1993. He received the B.S. degree and Ph.D. degree in electrical engineering from Zhejiang University, Hangzhou, China, in 2015 and 2020, respectively.
He is currently a postdoctoral researcher in Zhejiang University. His major research interests include the analytical modelling of PMSM and iron loss analysis.

Xiaoyan Huang (M'09) received the B.E. degree in control measurement techniques and instrumentation from Zhejiang University, Hangzhou, China, in 2003, and received the Ph.D. degree in electrical machines and drives from the University of Nottingham, Nottingham, U.K., in 2008.

From 2008 to 2009, she was a Research Fellow with the University of Nottingham. Currently, she is a professor with the College of Electrical Engineering, Zhejiang University, China, where she is working on electrical machines and drives. Her research interests are PM machines and drives for aerospace and traction applications, and generator system for urban networks.

L.J. Wu (M'11-SM'14) received the B.Eng. and M.Sc. degrees from Hefei University of Technology, Hefei, China, in 2001 and 2004, respectively, and the Ph.D degree from the University of Sheffield, Sheffield, U.K., in 2011, all in electrical engineering.

Since 2016, he has been with Zhejiang University, where he is currently Professor of electrical machines and control systems. His current research interests include design and control of PM machines.

He Zhang (M'14–SM'18) received the B.Eng. degree in control science and engineering from Zhejiang University, Hangzhou, China, in 2002, and the M.Sc. and Ph.D. degrees in electrical machines from the University of Nottingham, Nottingham, U.K., in 2004 and 2009, respectively.

He is currently the Director with the Nottingham Electrification Centre, Power Electronics, Machines, and Control Research Group, University of Nottingham. His research interests include high-performance electric machines and drives for transport electrification.

Tingna Shi (M'13) was born in Yuyao, China, in 1969. She received the B. S. and M. S. degrees from Zhejiang University, China, in 1991 and 1996 respectively, and the Ph.D. degree from Tianjin University, China, in 2009, all in electrical engineering.

She is currently a Professor with the College of Electrical Engineering, Zhejiang University, Hangzhou, China. Her current research interests include electrical machines and their control systems, power electronics, and electric drives.

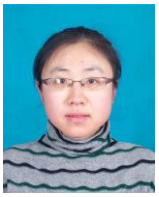

Yan Yan was born in Tianjin, China, in 1981. She received the B.S. and M.S. degrees from Tianjin University of Science and Technology, Tianjin, China, in 2004 and 2007, respectively, and the Ph.D. degree from Tianjin University, Tianjin, China, in 2010, all in electrical engineering.
She is currently an Associate Professor with the College of Electrical Engineering, Zhejiang University, Hangzhou, China. Her current research interests include electrical machines and their control systems, power electronics, and electric drives.

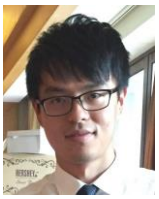

Bowen Shi was born in Hangzhou, China, in 1990. He received his B.S. and Ph.D degree in electrical engineering from University of Nottingham in 2013 and 2018, respectively. He is working as Senior Engineer in Nottingham Electrification Center and postdoctoral researcher in Zhejiang University. His main research interest is the PMSM design for traction applications.

Geng Yang received his BSc and MSc degrees from the College of Biomedical Engineering and Instrument Science, Zhejiang University (ZJU), Hangzhou, China, in 2003 and 2006 respectively; and the Ph.D. degree from Electronic and Computer Systems from the Royal Institute of Technology (KTH), Stockholm, Sweden in 2013.

Currently, he is a Research Professor in School of Mechanical Engineering, Zhejiang University, Hangzhou, China. He developed low power, low noise bio-electric SoC sensors for m-health. His research interests include flexible and stretchable electronics, mixed-mode IC design, low-power biomedical microsystem, wearable bio-devices, human-computer interface, human-robot interaction, intelligent sensors and Internet-of-Things for healthcare.